

First appearance of quasiprobability negativity in quantum many-body dynamics

Rohit Kumar Shukla,^{1, 2, 3, *} xxx,⁴ and Amikam Levy^{1, 2, 3, †}

¹*Department of Chemistry, Bar-Ilan University, Ramat-Gan 52900, Israel*

²*Institute of Nanotechnology and Advanced Materials, Bar-Ilan University, Ramat-Gan 52900, Israel*

³*Center for Quantum Entanglement Science and Technology, Bar-Ilan University, Ramat-Gan 52900, Israel*

⁴*xxx*

(Dated: November 20, 2025)

Quasiprobability distributions capture aspects of quantum dynamics that have no classical counterpart, yet their emergence in real time within many-body systems remains largely unexplored. We introduce the *first-time negativity* (FTN) of the Margenau-Hill quasiprobability as a dynamical indicator of when local measurement sequences in an interacting quantum system begin to exhibit genuinely nonclassical behavior. Using the Ising chain, we show that FTN discriminates clearly between interaction-dominated and field-dominated regimes, is systematically reshaped by temperature, and responds sensitively to the breaking of integrability. When measurements are performed on different sites, FTN reveals a characteristic spatio-temporal structure that reflects the finite-time spreading of operator incompatibility across the lattice. We further compare the numerical onset of negativity with a recently proposed quantum speed limit (QSL) for quasiprobabilities, which provides a kinematic benchmark for the observed dynamics. Our results identify FTN as a practical and experimentally accessible probe of real-time quantum coherence and contextuality, directly suited to current platforms capable of sequential weak and strong measurements.

I. INTRODUCTION

Quasiprobability distributions extend classical probability theory to describe genuinely quantum features such as interference, contextuality, and the effects of noncommuting observables. Unlike ordinary probabilities, they may take negative or even complex values, while still reproducing the correct marginals for physical measurements. In continuous-variable systems, this role is played by phase-space distributions such as the Wigner, Glauber-Sudarshan, and Husimi functions [1–4], whose negativity has long been recognized as a marker of nonclassicality [5]. For discrete systems, the Kirkwood-Dirac quasiprobability (KDQ) [6–9] provides a joint distribution for incompatible observables. Its real part, the Margenau-Hill quasiprobability (MHQ) [10], has been developed in foundational, thermodynamic and information-theoretic settings [11–22] and is directly accessible in experiment via weak-then-strong measurement schemes [8, 22–24].

In this framework, nonpositivity of the KDQ/MHQ is a particularly stringent sign of nonclassicality. Noncommutativity alone does not guarantee negativity [19, 25]: negative values arise only when sequential statistics cannot be reproduced by any noncontextual hidden-variable model [17, 26]. The imaginary part of the KDQ is linked to measurement back-action and disturbance [23, 27–31], while its negativity has been connected to advantages in metrology and thermodynamics [13, 18, 32–34], to work statistics in many-body systems [35–37], and to nonclassical signatures in projective-measurement protocols [15, 24, 37]. Quasiprobabilities thus provide a unified

language for quantifying “how quantum” a given dynamical process is, beyond what can be inferred from standard correlation functions alone.

A natural yet largely unexplored question is *when* such nonclassicality first appears in time. In other words, given a many-body system, a choice of local observables, and an initial state, what is the earliest time at which the corresponding quasiprobability distribution must cease to be nonnegative? Recent work has derived a QSL that bounds from below the time at which KDQ entries can become nonpositive [38]. However, this bound is constructed for a single pair of projectors and need not be saturated by the actual dynamics; in particular, it may be finite even when the associated quasiprobability remains nonnegative for all times. This suggests that the true onset of negativity is controlled not only by kinematic constraints, but also by the detailed structure of the Hamiltonian and the chosen observables.

In this work we address this dynamical question in a paradigmatic interacting system: a one-dimensional Ising chain with transverse and longitudinal fields. We focus on local, experimentally accessible probes and on the Margenau-Hill quasiprobability associated with sequential measurements of single-qubit Pauli operators. As our main diagnostic we introduce the *first-time negativity* (FTN), t_{FTN} , defined as the earliest time at which any Margenau-Hill (MH) entry becomes negative for a given pair of local projectors. This quantity provides a sharp operational timescale for the onset of contextual quantum interference in sequential measurements. We study how t_{FTN} depends on the transverse field, on temperature, on integrability breaking by a longitudinal field, and on the spatial separation between measurement sites.

Our analysis reveals several robust features. In the integrable transverse-field Ising model, initialized in its ground state, MH negativity appears only for σ_z

* rohitkrshukla.rs.phy17@itbhu.ac.in

† amikam.levy@biu.ac.il

probes. The corresponding FTN exhibits distinct asymptotic scalings in the interaction-dominated and field-dominated regimes and is essentially independent of system size, confirming its local character. Finite temperature progressively broadens the sharp zero-temperature feature around the quantum critical point into a finite-temperature crossover and eventually suppresses negativity in the high-temperature, fully mixed limit. Comparison with the KDQ-based QSL shows that the bound captures only the maximal kinematic rate of change: it can predict a finite minimal time to *possible* nonpositivity even in regimes where the MH quasiprobability remains nonnegative at all times, whereas the FTN directly tracks the actual emergence of negativity.

Breaking integrability by adding a longitudinal field lifts the symmetry that protected σ_x from generating negativity, so that both σ_z and σ_x observables develop non-classical quasiprobabilities. Extending the construction to projectors on different lattice sites, we uncover a clear spatio-temporal structure: the FTN grows with distance, reflecting the finite propagation time required for incompatibility to build up between measurements at distinct positions. Together, these results show that the FTN of the Margenau-Hill quasiprobability offers a concise, experimentally relevant measure of when and where contextual quantum behavior becomes unavoidable in many-body dynamics [39], complementary to more traditional diagnostics such as correlators and out-of-time-ordered functions.

The remainder of this paper is organized as follows. In Sec. II we introduce the Ising spin model and define the Margenau-Hill quasiprobability, its negativity, and the associated first-time negativity t_{FTN} , together with the relevant quantum speed-limit bound. Section III presents our main results: we first analyse the integrable transverse-field case at zero and finite temperature, and then study the nonintegrable regime with a longitudinal field and with measurements on spatially separated sites. In Sec. IV we summarize our findings and discuss possible extensions to other models.

II. THEORETICAL FRAMEWORK

Ising spin system

We consider a one-dimensional Ising chain of N qubits with open boundaries, described by

$$H = -J \sum_{n=1}^{N-1} \sigma_n^x \sigma_{n+1}^x - h_z \sum_{n=1}^N \sigma_n^z - h_x \sum_{n=1}^N \sigma_n^x, \quad (1)$$

where J denotes the nearest-neighbour exchange, and h_z and h_x are transverse and longitudinal fields, respectively. We set $\hbar = 1$ throughout.

This model captures the competition between ferromagnetic exchange along the x direction, a transverse

field polarizing the spins along z , and an additional longitudinal field aligning them along x . The interplay between the transverse field h_z and the exchange coupling J governs the magnetic phase structure: for $h_x = 0$, the model exhibits a quantum phase transition at $h_z/J = 1$, separating a ferromagnetic ground state ($h_z/J < 1$) from a paramagnetic one ($h_z/J > 1$) [40]. Introducing a finite longitudinal field h_x breaks the integrability of the transverse-field Ising model, rounding the sharp transition into a crossover [41]. The resulting dynamics depend sensitively on the full set of parameters (J, h_z, h_x), and are generically chaotic away from fine-tuned limits or low-energy sectors.

In the following we will often focus on local qubit operators such as σ_i^z . Their two-time correlations and associated quasiprobabilities provide a direct probe of the distinct dynamical regimes of the model.

Quasiprobability distributions and negativity

Local, single-site probes are directly accessible in today's platforms (trapped ions [42], Rydberg arrays, superconducting qubits [43], NV centers[44]). We therefore diagnose dynamical nonclassicality using a *local* two-time quasiprobability that can be reconstructed by weak and then strong sequential measurements on a single qubit.

Let V and W be observables with projectors $\{\Pi_\gamma\}$ and $\{\Xi_\delta\}$ on a single qubit. When acting on sites m and n of an N -qubit chain, the projectors are embedded into the full Hilbert space as $\Pi_\gamma^m \equiv \mathbb{I}^{\otimes m-1} \otimes \Pi_\gamma \otimes \mathbb{I}^{\otimes N-m}$ and $\Xi_\delta^n \equiv \mathbb{I}^{\otimes n-1} \otimes \Xi_\delta \otimes \mathbb{I}^{\otimes N-n}$. The KD quasiprobability for the ordered sequence “measure W at $t=0$ ” then “measure V at time t ” is

$$p_{\gamma\delta}^{mn}(t) = \text{Tr}[\Pi_\gamma^m(t) \Xi_\delta^n \rho_0], \quad \Pi_\gamma^m(t) = e^{iHt} \Pi_\gamma^m e^{-iHt}. \quad (2)$$

Here, ρ_0 is the initial state of the many-body system, taken as the ground state of the Hamiltonian. The real part of the KD quasiprobability, $q_{\gamma\delta}^{mn}(t) \equiv \text{Re } p_{\gamma\delta}^{mn}(t)$, is the MH quasiprobability [10], which will be our focus. Although not a genuine probability distribution, $q_{\gamma\delta}^{mn}(t)$ has consistent marginals: summing over one index yields the correct distribution for the other observable, and weighted sums reconstruct expectation values and two-time correlators. When the two projectors commute, $q_{\gamma\delta}^{mn}(t) \geq 0$ and coincides with an ordinary joint probability. By contrast, *negative* values can arise only if the sequential measurements are incompatible; such negativity reflects interference between different time orderings and, under standard operational assumptions (in particular, that weak pre-measurements are operationally non-invasive) [17, 26], rules out any noncontextual hidden-variable model reproducing the same sequential statistics.

For an N -qubit chain of Hilbert-space dimension $d = 2^N$, each local projector Π_γ^m or Ξ_δ^n has rank $d/2$, since it acts only on a single site. Consequently, the

KD elements $q_{\gamma\delta}^{mn}(t)$ capture interference between $d/2$ -dimensional subspaces rather than rank-1 rays. This coarse-grained setting is natural for local qubit readout and still admits quasiprobability negativity (and the associated contextuality certification), although coarse-graining can reduce the observed magnitude of negativity compared with a fully nondegenerate (rank-1) refinement.

We quantify the extent of negativity [16, 19] by

$$\mathcal{N}^{mn}(t) = \sum_{\gamma,\delta} \left| q_{\gamma\delta}^{mn}(t) \right| - 1, \quad (3)$$

and define the *first-time negativity* (FTN) as the earliest time when any MH entry turns negative,

$$t_{\text{FTN}}^{mn} = \min \left\{ t > 0 : \exists \gamma, \delta \text{ with } q_{\gamma\delta}^{mn}(t) < 0 \right\}. \quad (4)$$

First-time negativity and the quantum speed limit.

The central dynamical scale we extract is the first-time negativity t_{FTN}^{mn} in Eq. (4), i.e., the earliest instant when a quasiprobability entry becomes negative. This time directly marks the onset of contextual quantum interference. It is natural to ask how fast such a violation of classicality can possibly occur. Recent work [38] has derived a QSL for nonpositivity of KD quasiprobabilities, which provides a lower bound on t_{FTN}^{mn} . In our notation, the bound for the MHQ reads (see App. D)

$$T_{\gamma\delta;mn}^{\text{re}} = \frac{\tau(\rho_{\delta}^n, 0) - \tau(\rho_{\delta}^n, q_{\gamma\delta}^{mn}(0))}{\Delta L_{\gamma}^m}, \quad (5)$$

where $\rho_{\delta}^n = \{\rho_0, \Xi_{\delta}^n\}/2$, ΔL_{γ}^m is the standard deviation of the symmetric logarithmic derivative associated with $\Pi_{\gamma}^m(t)$, and $\tau(\rho_{\delta}^n, x)$ maps the expectation value x into an “angle” between the extremal eigenvalues of ρ_{δ}^n [45]. Physically, the denominator sets the maximal rate at which $q_{\gamma\delta}^{mn}(t)$ can change, while the numerator gives the distance it must travel to reach zero from its initial value. Thus $T_{\gamma\delta;mn}^{\text{re}}$ acts as a fundamental lower bound on t_{FTN}^{mn} . In the following we use it only as a benchmark: the QSL captures a universal kinematic constraint, whereas the actual t_{FTN}^{mn} reflects the concrete dynamical processes of the Ising chain.

Quantumness beyond correlations.

Two-time correlators such as $C_{VV}(t) = \langle V(t)V(0) \rangle$ diagnose memory and relaxation and can often be reproduced by classical stochastic dynamics with suitable kernels [46]. By contrast, MH negativity does not quantify the magnitude of correlations; it certifies the impossibility of describing the two sequential outcomes by any single, nonnegative, context-independent joint distribution [26, 47]. Consequently, $\mathcal{N}^{mn}(t)$ and t_{FTN}^{mn} diagnose

the onset of contextual quantum interference, whereas the correlator $C_{VV}(t)$ reflects the persistence of classical memory. In the Ising chain, these scales need not coincide; symmetry, locality, and operator growth can delay interference even when $C_{VV}(t)$ has already decayed or vice versa.

III. RESULTS

We present results for both the integrable transverse-field Ising chain ($h_x = 0$) and its nonintegrable extension with a finite longitudinal field ($h_x \neq 0$). The open boundary conditions break translational invariance, leading the FTN to vary with the spatial location of the measured observables. Unless noted otherwise, we focus on boundary sites, which for small transverse fields h_z exhibit a systematically longer t_{FTN} than sites in the bulk. This follows from locality: at an edge, the Heisenberg growth of a local projector proceeds through a single bond (one commutator channel) and spreads only inward, whereas in the bulk it spreads to both neighbours. The reduced spreading and fewer interfering paths at the boundary delay the build-up of the MHQ negativity (and similarly enlarge the QSL), an effect most pronounced in the ferromagnetic regime where interaction-driven string growth controls the dynamics. A full comparison of position dependence is provided in Appendix A.

Transverse-field Ising model

In the transverse-field Ising chain ($h_x = 0$) with the system initially prepared in its ground state, we find that among all single-qubit observables only σ_z exhibits quasiprobability negativity. The relevant quasiprobability is defined in terms of the local projectors $\Pi_0 = |0\rangle\langle 0|$ and $\Pi_1 = |1\rangle\langle 1|$ on site m and their time evolution $\Pi_{\gamma}^m(t)$ as described above. These projectors form the underlying KD distribution from which physical observables can be reconstructed.

In particular, the local change in polarization along the transverse field reads as

$$\Delta \langle \sigma_z^m(t) \rangle = \sum_{\gamma,\delta=0}^1 (\lambda_{\gamma} - \lambda_{\delta}) q_{\gamma\delta}^{mm}(t), \quad (6)$$

while higher moments follow from analogous combinations of KD entries. Similarly, the two-time autocorrelation function of the transverse polarization can be expressed as

$$\text{Re } C_{\sigma_z^m \sigma_z^m}(t) = \sum_{\gamma,\delta=0}^1 \lambda_{\gamma} \lambda_{\delta} q_{\gamma\delta}^{mm}(t), \quad (7)$$

with eigenvalues $\lambda_0 = -1$ and $\lambda_1 = 1$.

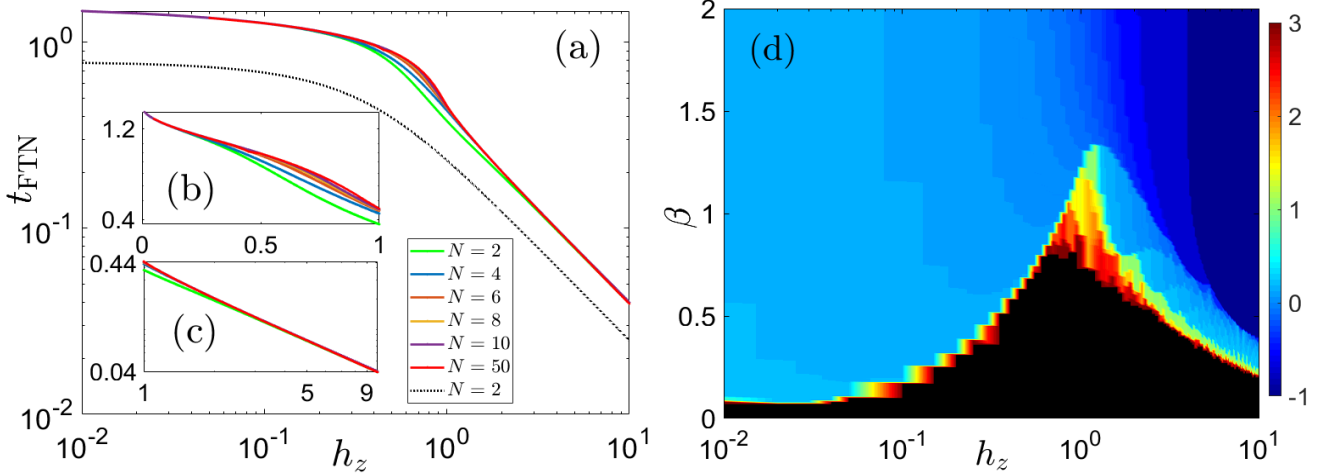


Figure 1. First-time negativity t_{FTN} (in units of $1/J$) for the integrable transverse-field Ising model ($h_x = 0$). (a) Zero temperature: t_{FTN} as a function of transverse field h_z for various system sizes (see legend), shown on a log-log scale with $J = 1$. The black dotted line indicates the quantum speed-limit bound t_{QSL} for $N = 2$. (b) Zero temperature: t_{FTN} vs. h_z in the range $h_z \in [10^{-2}, 1]$, shown on a log-linear scale. (c) Zero temperature: t_{FTN} vs. h_z in the range $h_z \in [1, 10]$, shown on a log-log scale. (d) Finite temperature: $\log(t_{\text{FTN}})$ as a function of h_z and inverse temperature $\beta = 1/k_B T$ (with $k_B = 1$) for $N = 8$ and $J = 1$.

Zero temperature

Figure 1(a) shows the FTN, t_{FTN} , as a function of the transverse field h_z for the integrable transverse-field Ising model ($h_x = 0$) initialized in its ground state. The evolution time t_{FTN} marks the onset of contextual quantum interference, i.e., the first moment when the MH quasiprobability of σ_z^m acquires negative values. Its dependence on h_z reveals three distinct dynamical regimes, separated by the quantum critical point $h_z = J$.

Ferromagnetic regime ($h_z \ll J$). For weak transverse fields, the exchange interaction dominates and the ground state is nearly polarized along the x direction. In this limit, the projectors $\Pi_\gamma^m(t)$ remain almost commuting with Π_γ^m , so the KD distribution stays nonnegative and t_{FTN} diverges at $h_z = 0$. For small but finite h_z , weak spin precession gradually introduces incompatibility, leading to finite negativity after a delay that scales as (see App. B)

$$t_{\text{FTN}} \approx \frac{1}{J} \left(\frac{\pi}{2} - \sqrt{\frac{2h_z}{J}} \right), \quad (h_z \ll J), \quad (8)$$

showing a square-root decrease as the transverse field enhances quantum fluctuations [Fig. 1(b)]. At the boundaries, t_{FTN} is slightly longer than in the bulk since operator spreading can occur only through a single neighboring bond.

Paramagnetic regime ($h_z \gg J$). When the transverse field dominates, spins precess independently around the z axis and quantum interference develops rapidly. The onset time decreases algebraically as (see App. B)

$$t_{\text{FTN}} \approx \frac{\pi h_z}{J^2 + 8h_z^2} \simeq \frac{\pi}{8h_z}, \quad (h_z \gg J), \quad (9)$$

consistent with the $1/h_z$ slope observed in the log-log plot of Fig. 1(c). In this regime, the dynamics are set by the local precession frequency, and the FTN reflects the single-spin timescale rather than collective correlations.

Vanishing-negativity limits. Negativity disappears entirely in the two trivial limits. For $J = 0$, the Hamiltonian $H = -h_z \sum_i \sigma_i^z$ commutes with all σ_i^z , giving $\Pi_\gamma^m(t) = \Pi_\gamma^m$ and a strictly classical joint probability. For $h_z = 0$, the dynamics are governed solely by $J \sum_i \sigma_i^x \sigma_{i+1}^x$, which preserves parity and leaves σ_z^m block-diagonal; the MH distribution again remains nonnegative. In both cases, $t_{\text{FTN}} \rightarrow \infty$.

The collapse of curves for system sizes $N = 2-50$ confirms that t_{FTN} is a local quantity, largely unaffected by system size (see Appendix C for the exact calculation for general system size N). The dotted line in Fig. 1(a) represents the corresponding QSL bound, which provides a lower kinematic bound for the time at which the KD distribution can become nonpositive. The bound exhibits a similar trend in the different regimes as h_z varies and consistently lies below the numerically observed t_{FTN} , reflecting that the bound captures the minimal geometric rate of state-projector incompatibility, whereas the actual onset of negativity depends on dynamical details of the many-body evolution. Moreover, we note that the QSL bound, while informative about the maximal rate of change of expectation values, does not necessarily coincide with the emergence of nonclassicality: in cases where the underlying quasiprobability remains nonnegative at all times, the QSL still defines a finite evolution speed, but this motion occurs entirely within the classical domain of compatible observables (see App. D).

Finite temperature

We next examine how thermal fluctuations modify the onset of negativity. At finite temperature, the initial ground state is replaced by a Gibbs state,

$$\rho_0 = \frac{e^{-\beta H}}{Z}, \quad Z = \text{Tr}(e^{-\beta H}), \quad (10)$$

with inverse temperature $\beta = 1/k_B T$ (setting $k_B = 1$). Figure 1(d) shows the resulting t_{FTN} landscape as a function of both β and the transverse field h_z .

At low temperatures (large β), the behavior closely follows the zero-temperature limit: t_{FTN} decreases monotonically with increasing h_z , showing the familiar crossover between the interaction-dominated ($h_z \ll J$) and field-dominated ($h_z \gg J$) regimes. As temperature rises, however, thermal excitations begin to mask quantum coherence, reducing the interference required for the quasiprobability to become negative. This suppression is reflected by the growing black region in Fig. 1(d), where no negativity is detected. Physically, thermal mixing damps the off-diagonal components of ρ_0 , weakening the overlap between the noncommuting projectors Π_γ^m and $\Pi_\gamma^m(t)$ that give rise to negativity.

The sharp $T = 0$ transition around $h_z = J$ broadens into a smooth finite-temperature crossover. For $\beta\Delta \lesssim 1$, where $\Delta \sim |h_z - J|$ is the energy gap, thermal excitations populate both spin-alignment sectors, blurring the distinction between the ferromagnetic and paramagnetic regimes. From the data in Fig. 1(d), this broadening follows approximately $\beta|h_z - J| \simeq 0.4$, forming a thermal “fan” region whose width increases as β decreases.

Far from criticality, the relevant dynamical scale is no longer dictated by the many-body gap but by the rapid transverse oscillations induced by the strong field. In the limit $h_z \gg J$, the dominant field aligns the spins nearly along the z -axis, while the weaker exchange term J drives small transverse fluctuations that oscillate at a rate set by h_z . These fast oscillations limit the buildup of coherent interference responsible for the emergence of negativity, leading to a characteristic timescale $t_{\text{FTN}} \propto 1/h_z$. As temperature increases, thermal averaging over these rapid oscillations becomes effective once $k_B T \gtrsim h_z$, further suppressing the appearance of negativity even when the excitation gap remains large. Thus, both mechanisms, the thermal smearing of correlations near the critical region and the field-induced suppression of coherence at large h_z , jointly determine the shape and extent of the finite-temperature boundary in Fig. 1(d).

In the high-temperature limit ($\beta \rightarrow 0$), the Gibbs state approaches a fully mixed state, $\rho_0 \rightarrow \mathbb{I}/2^N$, which is completely incoherent and lacks any off-diagonal structure in the energy basis. In this limit, the KD distribution remains strictly nonnegative for all h_z , and t_{FTN} effectively diverges, signaling the disappearance of contextual quantum dynamics.

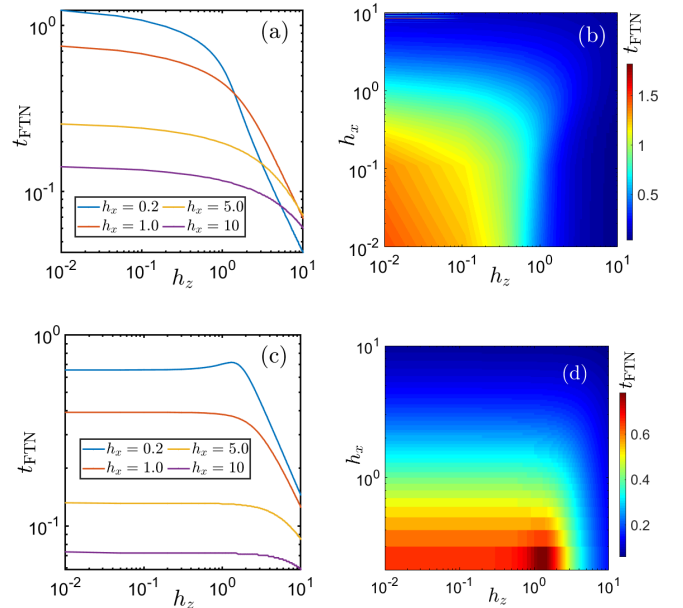


Figure 2. First-time negativity t_{FTN} (in units of $1/J$) in the nonintegrable Ising chain with a longitudinal field h_x . (a,c) t_{FTN} as a function of the transverse field h_z for several fixed values of h_x (see legends). (b,d) t_{FTN} as a function of both h_z and h_x . In panels (a,b) the local observable is $V = W = \sigma_z^1$, while in panels (c,d) it is $V = W = \sigma_x^1$. In all cases $N = 8$ and $J = 1$.

Nonintegrable case: longitudinal field

To explore the effect of breaking integrability, we now introduce a longitudinal field h_x into the Ising Hamiltonian. This term explicitly breaks the \mathbb{Z}_2 spin-flip symmetry of the transverse-field model [48], allowing additional local channels for generating quantum interference and hence quasiprobability negativity. Figures 2(a)-(d) summarize the dependence of the FTN on both h_x and h_z for two types of local projectors: panels (a,b) correspond to σ_z and panels (c,d) to σ_x observables. Unlike the integrable case, where the KD quasiprobability of σ_x remained strictly nonnegative, here both observables exhibit finite negativity once h_x is switched on.

For the σ_z projectors, Figs. 2(a),(b), the longitudinal field h_x preserves the overall qualitative shape of $t_{\text{FTN}}(h_z)$ but shifts it to shorter times. From the quasiprobability viewpoint, negativity requires coherent superpositions between the two σ_z eigenstates of the local spin. When $h_x = 0$, this mixing is generated only indirectly by the exchange term, so a boundary σ_z^m remains relatively protected and t_{FTN} is large, especially at small h_z . Turning on h_x adds a local σ_x term that does not commute with σ_z^m , creating such superpositions much more efficiently and thereby shortening t_{FTN} , as seen by the downward shift of the curves in Fig. 2(a) and the shrinking red region in the 2D map Fig. 2(b). For $h_z \gg J$, the strong transverse field domi-

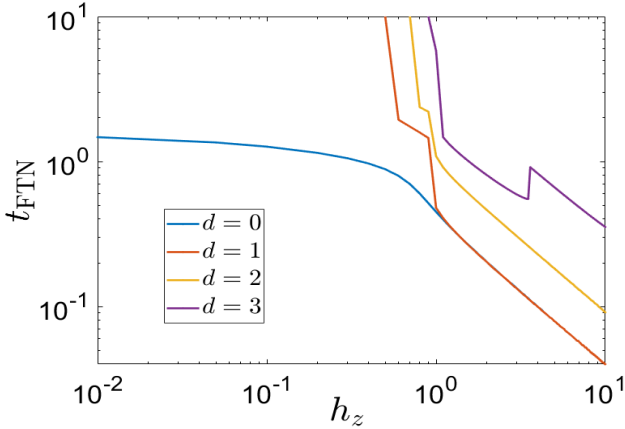


Figure 3. FTN t_{FTN} (in units of $1/J$) as a function of the transverse field h_z on a log-log scale in the integrable transverse-field Ising model. The quasiprobability is constructed from local observables $V = \sigma_z^m$ and $W = \sigma_z^n$, with $m = 1$ fixed and n varied from 1 to $N/2$ (so that $d = |n - m|$). Parameters: $J = 1$, $N = 8$, maximum simulation time 10^5 , and time step 10^{-3} .

ates the dynamics, and all curves collapse onto a common $t_{\text{FTN}} \propto 1/h_z$ tail with only weak residual dependence on h_x .

For the σ_x projectors, Figs. 2(c),(d), the introduction of h_x fundamentally changes the picture. At $h_x = 0$, the \mathbb{Z}_2 symmetry protects σ_x from generating negativity, leading to a purely classical KD distribution. Even a weak longitudinal field breaks this protection, allowing interference between parity sectors and yielding finite negativity. At small h_x , t_{FTN} is long and shows a shallow peak near $h_z \simeq J$, marking the transition between the interaction- and field-dominated regimes. As h_x increases, this feature disappears and t_{FTN} shortens throughout the entire range of h_z , reflecting a faster spread of operator incompatibility induced by the longitudinal perturbation. The color map in Fig. 2(d) confirms this trend: for a fixed h_z , larger h_x consistently leads to smaller t_{FTN} values. In the limit of large transverse fields, both σ_z and σ_x observables converge to the same asymptotic scaling $t_{\text{FTN}} \sim 1/h_z$, since the fast transverse rotations dominate over exchange and longitudinal contributions.

Spatio-temporal negativity at finite separation

So far, we have focused on local quasiprobabilities with $m = n$, which probe how nonclassicality develops in time at a single site. We now place the two projectors on different lattice sites and study the Margenau-Hill quasiprobability $q_{\gamma\delta}^{mn}(t)$ built from σ_z projectors at positions m and n . Operationally, $q_{\gamma\delta}^{mn}(t)$ encodes the sequential statistics of the process “measure σ_z^n at $t=0$, then σ_z^m at time t ”. Weighted sums over (γ, δ) reproduce spatio-temporal observables such as $\text{Re}\langle\sigma_z^m(t)\sigma_z^n(0)\rangle = \sum_{\gamma,\delta} \lambda_\gamma \lambda_\delta q_{\gamma\delta}^{mn}(t)$,

while the negativity of any entry rules out a single, non-negative, context-independent joint model for these sequential outcomes.

Figure 3 shows the FTN t_{FTN} in the integrable TFIM ($h_x = 0$) as a function of the transverse field h_z for a fixed reference site $m = 1$ and $n = 1+d$, with separations $d = |n - m|$ ranging from 0 to $N/2 - 1$. For very small transverse fields, the dynamics are dominated by the exchange term $-J \sum_i \sigma_i^x \sigma_{i+1}^x$. In this limit, a local operator such as σ_z^m spreads ballistically with a finite Lieb-Robinson velocity: outside the corresponding light cone, $\Pi_\gamma^m(t)$ has only an exponentially small overlap with site n , and the commutator $[\Pi_\gamma^m(t), \Pi_\delta^n]$ is exponentially suppressed. In this regime the MH quasiprobability is therefore extremely close to an ordinary joint probability and remains nonnegative within our numerical resolution. Consistent with this picture, for small h_z we do not observe any negativity within the maximal simulation time for the $d > 0$ curves.

For finite h_z , once $\Pi_\gamma^m(t)$ has spread across the bond structure to reach site n , the two projectors can become genuinely incompatible and negativity in $q_{\gamma\delta}^{mn}(t)$ becomes possible (it is a necessary yet not sufficient condition for negativity). This leads to a systematic increase of t_{FTN} with distance d : nonclassical sequential statistics at separation d appear only after a finite propagation time. As h_z approaches the critical value $h_z = J$, the group velocity of TFIM quasiparticles is maximized, and the light cone widens; correspondingly, $t_{\text{FTN}}(d)$ exhibits a pronounced drop near $h_z = J$, reflecting the faster spread of the incompatibility that underlies KD negativity.

In the strong-field regime $h_z \gg J$, the dynamics are dominated by the local field term, and the characteristic timescale for building up interference is set by the single-spin precession frequency. Consistent with the asymptotic expression Eq. (9), all curves collapse onto a common tail with $t_{\text{FTN}} \propto 1/h_z$ at large h_z , while remaining vertically offset by a distance-dependent delay associated with the time required for operator spreading between sites m and n . For larger separations d , small step-like features appear in $t_{\text{FTN}}(h_z)$, which are consistent with finite-size effects in the open chain, where discrete propagation across the lattice and reflections from the boundaries modulate the buildup of negativity.

IV. CONCLUSIONS

We have introduced the FTN of the Margenau-Hill quasiprobability as a dynamical marker for the onset of genuinely nonclassical behavior in many-body systems. Applied to the Ising chain, this quantity provides a sharp and operationally meaningful timescale at which sequential local measurements cease to admit any classical, non-contextual description.

In the integrable transverse-field model ($h_x = 0$), we showed that negativity emerges only for σ_z probes and that t_{FTN} displays two distinct dynamical regimes, sep-

erated by a sharp crossover around the quantum critical point $h_z = J$, governed respectively by interaction-dominated and field-dominated physics. Its weak dependence on system size highlights its local character, while its suppression at high temperature shows that thermal mixing both broadens the sharp zero-temperature feature around the quantum critical point into a finite-temperature crossover and can eventually wash out negativity altogether.

Comparison with the recently derived QSL for KD quasiprobabilities show that the bound captures only the maximal kinematic rate of change and can be finite even in regimes where the MH quasiprobability stays nonnegative at all times. By contrast, t_{FTN} captures the actual real-time onset of nonclassicality, in the concrete sense that it marks when negativity first appears in the quasiprobability.

Breaking integrability with a longitudinal field h_x lifts the symmetry protection that kept σ_x classical and activates new channels for generating superpositions. Both σ_z and σ_x observables then develop negativity, with a rich spatio-temporal structure that tracks how incompat-

ability propagates across the chain. The resulting t_{FTN} retains universal features, most notably a $1/h_z$ tail at strong fields, while revealing clear signatures of operator spreading and the altered dynamical landscape of the nonintegrable model.

Taken together, our results demonstrate that quasiprobability negativity provides a powerful, experimentally accessible probe of dynamical quantum behavior beyond correlations alone. The approach naturally extends to higher-dimensional systems, multitime sequences, and platforms capable of weak-and-strong measurement protocols, offering a new route to diagnosing the flow of quantum information in complex nonequilibrium settings.

ACKNOWLEDGMENTS

This research was supported by the ISF Grants No. 1364/21, 3105/23.

-
- [1] E. Wigner, On the quantum correction for thermodynamic equilibrium, *Physical review* **40**, 749 (1932).
 - [2] R. J. Glauber, Coherent and incoherent states of the radiation field, *Physical Review* **131**, 2766 (1963).
 - [3] E. Sudarshan, Equivalence of semiclassical and quantum mechanical descriptions of statistical light beams, *Physical Review Letters* **10**, 277 (1963).
 - [4] K. Husimi, Some formal properties of the density matrix, *Proceedings of the Physico-Mathematical Society of Japan. 3rd Series* **22**, 264 (1940).
 - [5] D. Walls, G. Milburn, D. Walls, and G. Milburn, Atomic optics, *Quantum Optics* , 315 (1994).
 - [6] J. G. Kirkwood, Quantum statistics of almost classical assemblies, *Physical Review* **44**, 31 (1933).
 - [7] P. A. M. Dirac, On the analogy between classical and quantum mechanics, *Reviews of Modern Physics* **17**, 195 (1945).
 - [8] M. Lostaglio, A. Belenchia, A. Levy, S. Hernández-Gómez, N. Fabbri, and S. Gherardini, Kirkwood-dirac quasiprobability approach to the statistics of incompatible observables, *Quantum* **7**, 1128 (2023).
 - [9] D. R. Arvidsson-Shukur, W. F. Braasch Jr, S. De Bievre, J. Dressel, A. N. Jordan, C. Langrenez, M. Lostaglio, J. S. Lundeen, and N. Y. Halpern, Properties and applications of the kirkwood-dirac distribution, *New Journal of Physics* **26**, 121201 (2024).
 - [10] H. Margenau and R. N. Hill, Correlation between measurements in quantum theory, *Progress of Theoretical Physics* **26**, 722 (1961).
 - [11] A. Barut, Distribution functions for noncommuting operators, *Physical Review* **108**, 565 (1957).
 - [12] L. M. Johansen, Quantum theory of successive projective measurements, *Physical Review A—Atomic, Molecular, and Optical Physics* **76**, 012119 (2007).
 - [13] A. E. Allahverdyan, Nonequilibrium quantum fluctuations of work, *Physical Review E* **90**, 032137 (2014).
 - [14] M. Lostaglio, Quantum fluctuation theorems, contextuality, and work quasiprobabilities, *Physical review letters* **120**, 040602 (2018).
 - [15] N. Yunger Halpern, B. Swingle, and J. Dressel, Quasiprobability behind the out-of-time-ordered correlator, *Physical Review A* **97**, 042105 (2018).
 - [16] J. R. González Alonso, N. Yunger Halpern, and J. Dressel, Out-of-time-ordered-correlator quasiprobabilities robustly witness scrambling, *Physical Review Letters* **122**, 040404 (2019).
 - [17] R. Kunjwal, M. Lostaglio, and M. F. Pusey, Anomalous weak values and contextuality: Robustness, tightness, and imaginary parts, *Physical Review A* **100**, 042116 (2019).
 - [18] A. Levy and M. Lostaglio, Quasiprobability distribution for heat fluctuations in the quantum regime, *PRX Quantum* **1**, 010309 (2020).
 - [19] D. R. Arvidsson-Shukur, J. C. Drori, and N. Y. Halpern, Conditions tighter than noncommutation needed for nonclassicality, *Journal of Physics A: Mathematical and Theoretical* **54**, 284001 (2021).
 - [20] J.-H. Pei, J.-F. Chen, and H. Quan, Exploring quasiprobability approaches to quantum work in the presence of initial coherence: Advantages of the margenau-hill distribution, *Physical Review E* **108**, 054109 (2023).
 - [21] V. Stepanyan and A. Allahverdyan, Energy densities in quantum mechanics, *Quantum* **8**, 1223 (2024).
 - [22] R. Wagner, Z. Schwartzman-Nowik, I. L. Paiva, A. Te’eni, A. Ruiz-Molero, R. S. Barbosa, E. Cohen, and E. F. Galvão, Quantum circuits for measuring weak values, kirkwood-dirac quasiprobability distributions, and state spectra, *Quantum Science and Technology* **9**, 015030 (2024).

- [23] J. T. Monroe, N. Yunger Halpern, T. Lee, and K. W. Murch, Weak measurement of a superconducting qubit reconciles incompatible operators, *Physical Review Letters* **126**, 100403 (2021).
- [24] S. Hernández-Gómez, S. Gherardini, A. Belenchia, M. Lostaglio, A. Levy, and N. Fabbri, Projective measurements can probe nonclassical work extraction and time correlations, *Physical Review Research* **6**, 023280 (2024).
- [25] S. De Bièvre, Complete incompatibility, support uncertainty, and kirkwood-dirac nonclassicality, *Physical Review Letters* **127**, 190404 (2021).
- [26] M. F. Pusey, Anomalous weak values are proofs of contextuality, *Physical review letters* **113**, 200401 (2014).
- [27] R. Jozsa, Complex weak values in quantum measurement, *Physical Review A—Atomic, Molecular, and Optical Physics* **76**, 044103 (2007).
- [28] H. F. Hofmann, On the role of complex phases in the quantum statistics of weak measurements, *New Journal of Physics* **13**, 103009 (2011).
- [29] J. Dressel and A. N. Jordan, Significance of the imaginary part of the weak value, *Physical Review A—Atomic, Molecular, and Optical Physics* **85**, 012107 (2012).
- [30] A. Budiyono and H. K. Dipojono, Quantifying quantum coherence via kirkwood-dirac quasiprobability, *Physical Review A* **107**, 022408 (2023).
- [31] S. Hernández-Gómez, T. Isogawa, A. Belenchia, A. Levy, N. Fabbri, S. Gherardini, and P. Cappellaro, Interferometry of quantum correlation functions to access quasiprobability distribution of work, *npj Quantum Information* **10**, 115 (2024).
- [32] M. Lostaglio, Certifying quantum signatures in thermodynamics and metrology via contextuality of quantum linear response, *Physical Review Letters* **125**, 230603 (2020).
- [33] J. H. Jenne and D. R. Arvidsson-Shukur, Quantum learnability is arbitrarily distillable, *arXiv preprint arXiv:2104.09520* (2021).
- [34] A. V. Mallik, L. M. Cangemi, A. Levy, and E. G. Dalla Torre, Probing quantum anomalous heat flow using mid-circuit measurements, *Advanced Quantum Technologies* , e00328 (2025).
- [35] A. Santini, A. Solfanelli, S. Gherardini, and M. Collura, Work statistics, quantum signatures, and enhanced work extraction in quadratic fermionic models, *Physical Review B* **108**, 104308 (2023).
- [36] G. Francica and L. Dell'Anna, Quasiprobability distribution of work in the quantum ising model, *Physical Review E* **108**, 014106 (2023).
- [37] S. Gherardini and G. De Chiara, Quasiprobabilities in quantum thermodynamics and many-body systems, *PRX Quantum* **5**, 030201 (2024).
- [38] S. S. Pratapsi, S. Deffner, and S. Gherardini, Quantum speed limit for kirkwood-dirac quasiprobabilities, *Quantum Science and Technology* **10**, 035019 (2025).
- [39] K. Yang, X. Zeng, Y. Luo, G. Yang, L. Shu, M. Navascués, and Z. Wang, Contextuality in infinite one-dimensional translation-invariant local hamiltonians, *npj Quantum Information* **8**, 89 (2022).
- [40] S. Sachdev, Quantum phase transitions, *Physics world* **12**, 33 (1999).
- [41] J. D. Noh, Operator growth in the transverse-field ising spin chain with integrability-breaking longitudinal field, *Physical Review E* **104**, 034112 (2021).
- [42] C. D. Bruzewicz, J. Chiaverini, R. McConnell, and J. M. Sage, Trapped-ion quantum computing: Progress and challenges, *Applied physics reviews* **6**, <https://doi.org/10.1063/1.5088164> (2019).
- [43] S. S. Elder, C. S. Wang, P. Reinhold, C. T. Hann, K. S. Chou, B. J. Lester, S. Rosenblum, L. Frunzio, L. Jiang, and R. J. Schoelkopf, High-fidelity measurement of qubits encoded in multilevel superconducting circuits, *Physical Review X* **10**, 011001 (2020).
- [44] M. Cambria, S. Chand, C. M. Reiter, and S. Kolkowitz, Scalable parallel measurement of individual nitrogen-vacancy centers, *Physical Review X* **15**, 031015 (2025).
- [45] Since the local projectors have rank $d/2$, we normalize Π_γ^m to unit trace for consistency with the convention in Ref. [38].
- [46] R. Carballera, D. Dolgitzer, P. Zhao, D. Zeng, and Y. Chen, Stochastic schrödinger equation derivation of non-markovian two-time correlation functions, *Scientific Reports* **11**, 11828 (2021).
- [47] D. Schmid, R. D. Baldijão, Y. Ying, R. Wagner, and J. H. Selby, Kirkwood-dirac representations beyond quantum states and their relation to noncontextuality, *Physical Review A* **110**, 052206 (2024).
- [48] M. Heyl, Dynamical quantum phase transitions: a review, *Reports on Progress in Physics* **81**, 054001 (2018).
- [49] E. Lieb, T. Schultz, and D. Mattis, Two soluble models of an antiferromagnetic chain, *Annals of Physics* **16**, 407 (1961).
- [50] A. D'Abbruzzo and D. Rossini, Topological signatures in a weakly dissipative kitaev chain of finite length, *Physical Review B* **104**, 115139 (2021).
- [51] M.-w. Xiao, Theory of transformation for the diagonalization of quadratic hamiltonians, *arXiv preprint arXiv:0908.0787* (2009).
- [52] Y. He and H. Guo, The boundary effects of transverse field ising model, *Journal of Statistical Mechanics: Theory and Experiment* **2017**, 093101 (2017).

Appendix A: Position Dependence of the FTN and QSL

We investigate how the spatial placement of local observables affects both the FTN and the QSL for the Kirkwood–Dirac quasiprobability. Open boundary conditions break translational invariance, so the timescale for the emergence of negativity depends explicitly on the positions of the measured sites.

We start by considering both observables located at the same boundary site, $m = n \in 1, N$. In this configuration, the FTN exhibits a pronounced dependence on the transverse field strength h_z , as discussed in the main text. To study spatial effects systematically, we progressively move the observables from the edge into the bulk, i.e., to positions $m = n = 2, 3, \dots, N - 1$.

A clear pattern emerges in the ferromagnetic regime ($h_z < J$): boundary observables display significantly larger FTN compared to bulk observables. In contrast, in the paramagnetic regime the FTN becomes nearly independent of position. Moreover, the FTN exhibits a mirror symmetry between sites m/n and $(N - m + 1)/(N -$

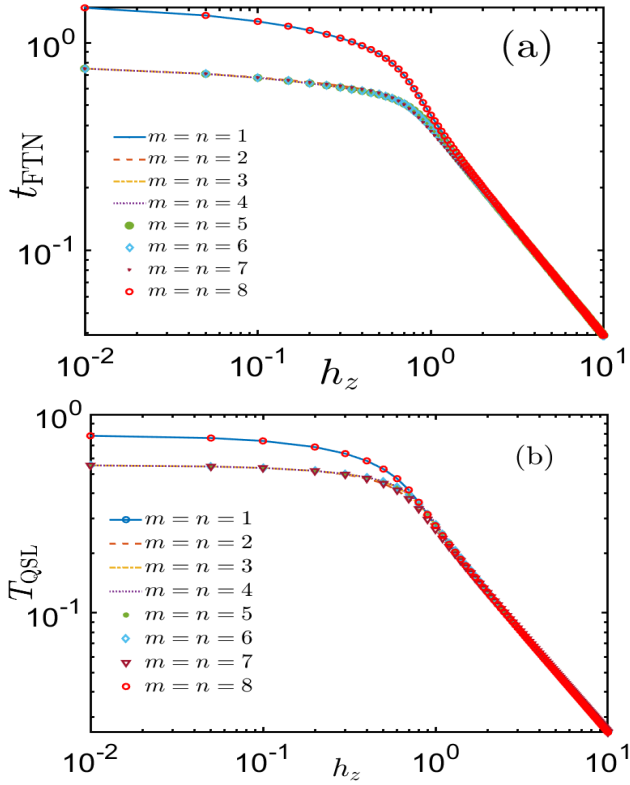


Figure 4. First-time negativity and quantum speed-limit time for boundary and bulk observables in the integrable transverse-field Ising model. (a) First-time negativity t_{FTN} as a function of the transverse field h_z for different single-site positions with $m = n$ (boundary and bulk, see legend). (b) Corresponding quantum speed-limit time T_{QSL} for the onset of possible nonpositivity of the KD quasiprobability, plotted under the same conditions. All data are at zero temperature, with $N = 8$, $J = 1$, and $h_x = 0$.

$n+1$) [Fig. 4(a)], a consequence of the spatial uniformity of the Hamiltonian, which renders correlations invariant under reflection about the chain center.

The physical origin of this boundary–bulk contrast can be traced to locality. At the edge, the Heisenberg evolution of a local projector spreads through only a single bond (one commutator channel), whereas in the bulk it propagates to two neighboring sites. This restricted spreading at the boundaries reduces the number of interfering operator paths, delaying the emergence of MHQ negativity and producing larger FTN. The effect is most pronounced in the ferromagnetic regime, where interaction-driven string growth dominates the dynamics.

To quantify the earliest time at which negativity appears, we compute the QSL time, T_{QSL} , following the procedure outlined in Appendix D. Evaluating T_{QSL} for projectors $|1\rangle\langle 1|$ at various positions $m = n$ using Eq. (5) reveals a strong correlation with the FTN. Boundary projectors take longer to become non-positive, whereas bulk projectors reach negativity more rapidly. As ex-

pected, T_{QSL} always provides a lower bound to the corresponding FTN. Additionally, T_{QSL} exhibits the same mirror symmetry as the FTN between sites m/n and $(N - m + 1)/(N - n + 1)$, as shown in Fig. 4(b).

These results highlight that boundary observables serve as especially sensitive probes of quantum correlations and operator growth. Their constrained spreading along the edges leads to enhanced FTN and delayed MHQ negativity, emphasizing the critical role of the system’s spatial structure in determining the spatio-temporal onset of contextual quantum behavior.

Appendix B: Asymptotic scaling of the FTN

An analytical expression for the quasiprobability for arbitrary system size N in the integrable transverse-field Ising model (TFIM) ($h_x = 0$) is derived in Appendix C. However, the resulting expressions become cumbersome for extracting explicit time dependence, since the time variable appears inside a cosine function that is also nested within a summation, i.e., $\sum_{k,p} C_{k,p} \cos [(\omega_p + \omega_k)t]$, making it challenging to observe clear trends of the FTN with respect to the transverse field h_z . To circumvent this difficulty, a simpler two-qubit model is considered. Remarkably, the FTN behavior is found to be approximately independent of system size, allowing insights gained from this minimal model to remain valid for larger systems. This toy model captures the essential physics, displaying a clear decreasing trend of the FTN with increasing transverse field strength in both the paramagnetic and ferromagnetic regimes of the TFIM. The corresponding two-qubit Hamiltonian is given by:

$$H = -J\sigma_1^x \otimes \sigma_2^x - h_z (\hat{\sigma}_1^z \otimes \mathbb{I} + \mathbb{I} \otimes \hat{\sigma}_2^z) \\ = \begin{bmatrix} -2h_z & 0 & 0 & -J \\ 0 & 0 & -J & 0 \\ 0 & -J & 0 & 0 \\ -J & 0 & 0 & 2h_z \end{bmatrix}. \quad (\text{B1})$$

Diagonalization of this Hamiltonian yields the eigenvalues E and eigenvectors V , which are essential for constructing the time evolution operator and the ground state:

$$E = \begin{pmatrix} -J & 0 & 0 & 0 \\ 0 & J & 0 & 0 \\ 0 & 0 & -\sqrt{4h_z^2 + J^2} & 0 \\ 0 & 0 & 0 & \sqrt{4h_z^2 + J^2} \end{pmatrix}, \\ V = \begin{pmatrix} 0 & 0 & -\frac{-\sqrt{4h_z^2 + J^2} - 2h_z}{J} & -\frac{\sqrt{4h_z^2 + J^2} - 2h_z}{J} \\ 1 & -1 & 0 & 0 \\ 1 & 1 & 0 & 0 \\ 0 & 0 & 1 & 1 \end{pmatrix}.$$

The spectrum consists of four energy levels, $\pm J$ and $\pm \sqrt{4h_z^2 + J^2}$, with the lowest energy level

$$E_0 = -\sqrt{4h_z^2 + J^2}$$

and the corresponding eigenvector defining the normalized ground state $|\Psi_0\rangle$:

$$|\Psi_0\rangle = \begin{bmatrix} \frac{2h_z + \sqrt{4h_z^2 + J^2}}{\sqrt{(\sqrt{4h_z^2 + J^2} - 2h_z)^2 + J^2}} \\ 0 \\ 0 \\ J \\ \sqrt{(\sqrt{4h_z^2 + J^2} + 2h_z)^2 + J^2} \end{bmatrix}. \quad (\text{B2})$$

The time evolution is governed by the unitary operator $U(t) = e^{-iHt}$. Its matrix representation in the computational basis is:

$$U(t) = \begin{pmatrix} \cos(t\sqrt{4h_z^2 + J^2}) + \frac{2ih_z \sin(t\sqrt{4h_z^2 + J^2})}{\sqrt{4h_z^2 + J^2}} & 0 \\ 0 & \cos(Jt) \\ 0 & i \sin(Jt) \\ \frac{iJ \sin(t\sqrt{4h_z^2 + J^2})}{\sqrt{4h_z^2 + J^2}} & 0 \\ 0 & \frac{iJ \sin(t\sqrt{4h_z^2 + J^2})}{\sqrt{4h_z^2 + J^2}} \\ i \sin(Jt) & 0 \\ \cos(Jt) & 0 \\ 0 & \cos(t\sqrt{4h_z^2 + J^2}) - \frac{2ih_z \sin(t\sqrt{4h_z^2 + J^2})}{\sqrt{4h_z^2 + J^2}} \end{pmatrix}$$

In the integrable TFIM, only the Pauli observables $V = W = \sigma_n^z$ contribute to negativity. Focusing on the boundary positions, $V = W = \sigma_1^z$, it is found that a single combination of projectors, $|1\rangle\langle 1|$, yields negative quasiprobability. This indicates that only this quasiprobability contributes to the calculation of FTN. The corresponding projectors are

$$\Xi_1^1 = \Pi_1^1 = \begin{bmatrix} 0 & 0 & 0 & 0 \\ 0 & 0 & 0 & 0 \\ 0 & 0 & 1 & 0 \\ 0 & 0 & 0 & 1 \end{bmatrix}, \quad (\text{B3})$$

with the quasiprobability defined as

$$q_{11}^{11}(t) = \langle \Psi_0 | \Pi_1^1(t) \Xi_1^1 | \Psi_0 \rangle. \quad (\text{B4})$$

After simplification, the real part is expressed as

$$\text{Re}[q_{11}^{11}(t)] = \frac{4h_z^2 - 2h_z \sqrt{4h_z^2 + J^2} + J^2 \cos^2(\sqrt{4h_z^2 + J^2} t)}{8h_z^2 + 2J^2}. \quad (\text{B5})$$

This provides the condition for the FTN, $\text{Re}[q_{11}^{11}(t)] \leq 0$, and allows analysis of its asymptotic behavior as the transverse field varies.

a. *Case I: $h_z \ll J$* : Defining the small parameter $\epsilon = h_z/J \ll 1$, expansion of the square root yields

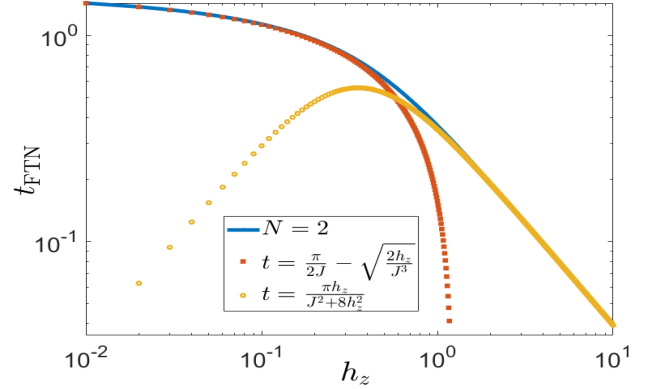


Figure 5. Exact and asymptotic behavior of the first-time negativity in the transverse-field Ising model for $N = 2$ and $J = 1$. The blue line shows the exact t_{FTN} as a function of the transverse field h_z . Orange squares indicate the weak-field approximation $t_{\text{FTN}} = \frac{\pi}{2J} - \sqrt{2h_z/J^3}$ (valid for $h_z \ll J$), and yellow circles indicate the strong-field approximation $t_{\text{FTN}} = \frac{\pi h_z}{J^2 + 8h_z^2}$ (valid for $h_z \gg J$).

$\sqrt{4\epsilon^2 + 1} \approx 1 + 2\epsilon^2$. Substituting into Eq. (B5) and solving for the time gives

$$t_{\text{FTN}} \equiv t \approx \frac{\pi}{2J} - \sqrt{\frac{2h_z}{J^3}}, \quad (\text{B6})$$

highlighting that the FTN is dominated by $1/J$ with a subleading correction proportional to $\sqrt{h_z/J^3}$.

b. *Case II: $h_z \gg J$* : For $\epsilon = J/h_z \ll 1$, the condition $\text{Re}[q_{11}^{11}(t)] = 0$ leads to

$$t_{\text{FTN}} \equiv t \approx \frac{\pi h_z}{J^2 + 8h_z^2} \approx \frac{\pi}{8h_z}, \quad (\text{B7})$$

showing that in the strong-field regime, the FTN scales asymptotically as $1/h_z$.

c. *Extreme limit $h_z \gg J$* : When J is negligible compared to h_z , $\text{Re}[q_{11}^{11}(t)] \geq 0$ for all t , indicating that the quasiprobability never becomes negative and the system behaves classically.

The asymptotic expressions in Eqs. (B6) and (B7) capture the scaling of the FTN in the weak- and strong-field limits and are consistent with numerical trends observed in the two-qubit system, as shown in Fig. 5.

Appendix C: Quasiprobability formula for a spin chain of arbitrary length N

The integrable TFIM can be diagonalized, which allows us to obtain the exact formula of quasiprobability. To do this, we first use the relations $\sigma_n^{x/z} = 2S_n^{x/z}$ and $S_n^\pm = S_n^x \pm iS_n^y$, so that $S_n^x = \frac{1}{2}(S_n^+ + S_n^-)$. Substituting S_n^x and $h_x = 0$ into Eq. (1), the spin Hamiltonian reduces

to

$$H = -J \sum_{n=1}^{N-1} (S_n^+ S_{n+1}^+ + S_n^+ S_{n+1}^- + S_n^- S_{n+1}^+ + S_n^- S_{n+1}^-) - 2h_z \sum_{n=1}^N S_n^z. \quad (\text{C1})$$

The spin operators can be expressed in terms of fermionic operators through the Jordan–Wigner transformation:

$$\begin{aligned} S_n^- &= \exp\left(i\pi \sum_{l=1}^{n-1} c_l^\dagger c_l\right) c_n, \\ S_n^+ &= c_n^\dagger \exp\left(-i\pi \sum_{l=1}^{n-1} c_l^\dagger c_l\right), \\ S_n^z &= c_n^\dagger c_n - \frac{1}{2}. \end{aligned} \quad (\text{C2})$$

For convenience, we introduce the non-local string operator

$$Q_n = \exp\left(i\pi \sum_{l=1}^{n-1} c_l^\dagger c_l\right) = \prod_{l=1}^{n-1} (1 - 2c_l^\dagger c_l), \quad (\text{C3})$$

which satisfies the properties $Q_n^\dagger = Q_n$, $Q_n^2 = 1$, and $Q_n Q_{n+1} = 1 - 2c_n^\dagger c_n$. Using this construction, the nearest-neighbor spin interactions can be expressed in fermionic form as

$$\begin{aligned} S_n^+ S_{n+1}^+ &= c_n^\dagger c_{n+1}^\dagger \\ S_n^+ S_{n+1}^- &= c_n^\dagger c_{n+1} \\ S_n^- S_{n+1}^+ &= -c_n c_{n+1}^\dagger \\ S_n^- S_{n+1}^- &= -c_n c_{n+1}. \end{aligned}$$

Thus, the spin Hamiltonian is fully mapped into a fermionic representation, yielding the compact quadratic form

$$\begin{aligned} H &= -J \sum_{n=1}^{N-1} (c_n^\dagger c_{n+1} + c_{n+1}^\dagger c_n + c_n^\dagger c_{n+1}^\dagger + c_{n+1} c_n) \\ &\quad - h_z \sum_{n=1}^N (2c_n^\dagger c_n - 1), \end{aligned} \quad (\text{C4})$$

Since the Hamiltonian is quadratic in the fermionic operators, it can be diagonalized using the Bogoliubov–Valatin (BV) transformation [49–52]:

$$c_n = \sum_k (A_{nk} b_k + B_{nk} b_k^\dagger), \quad (\text{C5})$$

where b_k and b_k^\dagger are new fermionic annihilation and creation operators. The matrices A and B (discussed later how to construct them), obtained via the Lieb–Schultz–Mattis (LSM) procedure, bring the Hamiltonian into the diagonal form

$$H = \sum_k \omega_k b_k^\dagger b_k + \text{const}, \quad (\text{C6})$$

with a real, nonnegative excitation spectrum given by

$$\omega_k^2 = 4J^2 + 8Jh_z \cos(k) + 4h_z^2, \quad (\text{C7})$$

The allowed values of k are determined by the boundary condition

$$J \sin(kN) + h_z \sin[k(N+1)] = 0. \quad (\text{C8})$$

Thus, the diagonalization requires both the eigenvalues ω_k [Eq. (C7)] and the quantization condition for k [Eq. (C8)]. In what follows, we outline the procedure to obtain these results.

Lieb–Schultz–Mattis Method: We are employing the LSM method to diagonalize the quadratic fermionic Hamiltonian, Eq. (C4), which is defined in terms of the real matrices Q_{mn} and P_{mn} :

$$H = \sum_{m,n=1}^N \left[Q_{mn} c_m^\dagger c_n + \frac{1}{2} P_{mn} (c_m^\dagger c_n^\dagger + c_n c_m) \right] + h_z N, \quad (\text{C9})$$

where the matrices Q_{mn} and P_{mn} are given explicitly by

$$Q_{mn} = \begin{bmatrix} -2h_z & -J & 0 & \cdots & 0 \\ -J & -2h_z & -J & \cdots & 0 \\ 0 & -J & -2h_z & \cdots & 0 \\ \vdots & \vdots & \vdots & \ddots & \vdots \\ 0 & 0 & 0 & \cdots & -2h_z \end{bmatrix}, \quad (\text{C10})$$

$$P_{mn} = \begin{bmatrix} 0 & -J & 0 & \cdots & 0 \\ J & 0 & -J & \cdots & 0 \\ 0 & J & 0 & \cdots & 0 \\ \vdots & \vdots & \vdots & \ddots & \vdots \\ 0 & 0 & 0 & \cdots & 0 \end{bmatrix}. \quad (\text{C11})$$

The inverse BV transformation, with $X = A^T$ and $Y = B^T$, reads

$$b_k = \sum_{n=1}^N (X_{kn} c_n + Y_{kn} c_n^\dagger), \quad (\text{C12})$$

Expressing this in terms of the vectors $\mathbf{X}_k^T = (X_{k1}, \dots, X_{kN})$ and $\mathbf{Y}_k^T = (Y_{k1}, \dots, Y_{kN})$ leads to the consistency relations

$$Q\mathbf{X}_k + P\mathbf{Y}_k = \omega_k \mathbf{X}_k, \quad (\text{C13a})$$

$$-Q\mathbf{X}_k - P\mathbf{Y}_k = \omega_k \mathbf{Y}_k. \quad (\text{C13b})$$

Introducing $\phi_k = \mathbf{X}_k + \mathbf{Y}_k$ and $\psi_k = \mathbf{X}_k - \mathbf{Y}_k$, these equations can be recast as

$$(Q + P)\phi_k = \omega_k \psi_k, \quad (\text{C14a})$$

$$(Q - P)\psi_k = \omega_k \phi_k. \quad (\text{C14b})$$

From this, a standard eigenvalue problem emerges:

$$V\phi_k = \omega_k^2 \phi_k, \quad (\text{C15a})$$

$$W\psi_k = \omega_k^2 \psi_k, \quad (\text{C15b})$$

with $V = (Q - P)(Q + P)$ and $W = (Q + P)(Q - P)$, these can be expressed in matrix form as follows:

$$V = \begin{pmatrix} 4h_z^2 & 4Jh_z & 0 & \cdots & 0 \\ 4Jh_z & 4J^2 + 4h_z^2 & 4Jh_z & \cdots & 0 \\ 0 & 4Jh_z & 4J^2 + 4h_z^2 & \cdots & 0 \\ \vdots & \vdots & \vdots & \ddots & 4Jh_z \\ 0 & 0 & 0 & 4Jh_z & 4J^2 + 4h_z^2 \end{pmatrix},$$

$$W = \begin{pmatrix} 4J^2 + 4h_z^2 & 4Jh_z & 0 & \cdots & 0 \\ 4Jh_z & 4J^2 + 4h_z^2 & 4Jh_z & \cdots & 0 \\ 0 & 4Jh_z & 4J^2 + 4h_z^2 & \cdots & 0 \\ \vdots & \vdots & \vdots & \ddots & 4Jh_z \\ 0 & 0 & 0 & 4Jh_z & 4h_z^2 \end{pmatrix}.$$

From the structure of these matrices, it follows that ϕ_k is related to ψ_k through an index inversion $n \rightarrow N+1-n$. Hence, it is sufficient to solve for ψ_k by determining the eigenvalues and eigenvectors of W . The corresponding eigenvalue equation leads to the following system:

$$4Jh_z(\psi_k)_{n-1} + (4J^2 + 4h_z^2)(\psi_k)_n + 4Jh_z(\psi_k)_{n+1} = \omega_k^2(\psi_k)_n, \quad 2 \leq n \leq N-1, \quad (\text{C16a})$$

$$(4J^2 + 4h_z^2)(\psi_k)_1 + 4Jh_z(\psi_k)_2 = \omega_k^2(\psi_k)_1, \quad (\text{C16b})$$

$$4Jh_z(\psi_k)_{N-1} + 4h_z^2(\psi_k)_N = \omega_k^2(\psi_k)_N. \quad (\text{C16c})$$

Equation (C16a) governs the bulk dynamics, while Eqs. (C16b) and (C16c) enforce the left and right boundary conditions, respectively. To solve the bulk equation, we assume a translationally invariant ansatz

$$(\psi_k)_n = -iC_k \frac{1}{2} (e^{ikn} + \alpha_k e^{-ikn}), \quad (\text{C17})$$

where k is the quantum number (possibly complex), and C_k , α_k are parameters. Using the boundary conditions, one finds $\alpha_k = -1$, leading to

$$\psi_{nk} = C_k \sin(kn), \quad (\text{C18a})$$

$$\phi_{nk} = D_k \sin[k(N+1-n)], \quad (\text{C18b})$$

where C_k and D_k are normalization constants related through

$$C_k^2 = D_k^2, \quad (\text{C19a})$$

$$\frac{2}{D_k^2} = N - \frac{\sin(kN)}{\sin k} \cos[k(N+1)], \quad (\text{C19b})$$

$$\frac{D_k}{C_k} = -\frac{2h_z \sin k}{\omega_k \sin(kN)}. \quad (\text{C19c})$$

These conditions imply that $C_k = \pm D_k$, with the relative sign depending on k , h_z , and N . Substituting function $(\psi_k)_n$ in Eq. (C16a) yields the eigenvalues ω_k^2 as in Eq. (C7), while the substituting function $(\psi_k)_n$ and value of ω_k^2 in right boundary condition [Eq. (C16c)] leads to the quantization condition defined in Eq. (C8).

The time evolution operator is

$$U = e^{-iHt} = e^{-i \sum_k \omega_k b_k^\dagger b_k t}.$$

In the integrable TFIM, only the Pauli operators $V = W = \sigma_n^z$ contribute to negative values of the quasiprobability. Among all possible combinations of projectors for these operators, only the combination where both projectors are $|1\rangle\langle 1|$ yields a negative quasiprobability. Consequently, this is the only quasiprobability that contributes to the calculation of the FTN. The projectors, expressed in terms of fermionic operators, are given by

$$\Pi_n^1 \equiv \Xi_n^1 = \frac{1}{2}(\mathbb{I} - \sigma_n^z) = \mathbb{I} - c_n^\dagger c_n = c_n c_n^\dagger. \quad (\text{C20})$$

Using these projectors, the quasiprobability can be expressed as

$$q_{11}^{nn}(t) = \langle \Psi_0 | \Pi_1^n(t) \Xi_1^n | \Psi_0 \rangle = \langle \Psi_0 | c_n(t) c_n^\dagger(t) c_n c_n^\dagger | \Psi_0 \rangle =$$

$$\langle \Psi_0 | \left[\sum_{k,k'} \left(A_{nk} A_{nk'}^* b_k(t) b_{k'}^\dagger(t) + A_{nk} B_{nk'}^* b_k(t) b_{k'}'(t) \right) \right.$$

$$\left. + B_{nk}^* A_{nk'}^* b_k^\dagger(t) b_{k'}^\dagger(t) + B_{nk} B_{nk'}^* b_k^\dagger(t) b_{k'}'(t) \right] | \Psi_0 \rangle \quad (\text{C21})$$

The time-evolved fermionic creation and annihilation operator is obtained by:

$$b_k^\dagger(t) = e^{i\omega_k t} b_k^\dagger, \quad \text{and} \quad b_k(t) = e^{-i\omega_k t} b_k. \quad (\text{C22})$$

Taking the expectation value with respect to the fermionic ground state $|\Psi_0\rangle = \prod_{k, E_k \leq E_F} b_k^\dagger |0\rangle$, and taking the real part, we have

$$\text{Re}[\langle \Psi_0 | \Pi_1^n(t) \Xi_1^n | \Psi_0 \rangle] = \sum_{k,p} |A_{nk}|^2 |A_{np}|^2$$

$$+ \sum_{k,p} (|A_{np}|^2 |B_{nk}|^2 - A_{np}^* B_{nk} B_{np}^* A_{nk}) \cos[(\omega_p + \omega_k)t]. \quad (\text{C23})$$

This equation is useful for the calculation of the quasiprobability for a general N .

To determine the time at which the quasiprobability first becomes negative, we set the real part of the expression equal to zero. This yields the condition

$$\sum_{k,p} C_{k,p} \cos[(\omega_p + \omega_k)t] = - \sum_{k,p} |A_{nk}|^2 |A_{np}|^2.$$

where $C_{k,p} = |A_{np}|^2 |B_{nk}|^2 - A_{np}^* B_{nk} B_{np}^* A_{nk}$. Since the time variable t appears inside the summations through oscillatory terms of the form $(\omega_p + \omega_k)$, the resulting expression does not admit a closed-form solution for its time dependence. As a result, it is challenging to extract the precise behavior of the negativity onset as the external transverse field h_z is varied.

Appendix D: Quantum speed limit - time to Non-Positivity in KD Quasiprobability

To bound the real part of the KDQ, we define the Hermitian operator

$$\rho_\delta^n \equiv \frac{\{\rho_0, \Xi_\delta^n\}}{2}, \quad (\text{D1})$$

which is time-independent. Using this operator, the real part of the KDQ, defined in Eq. (2), can be written as

$$q_{\delta,\gamma}^{mn}(t) \equiv \text{Re}[\rho_{\delta,\gamma}^{mn}(t)] = \text{Tr}[\rho_\delta^n \Pi_\gamma^m(t)] \equiv \langle \rho_\delta^n \rangle_{\gamma,t}^m, \quad (\text{D2})$$

which behaves like the expectation value of ρ_δ^n with respect to the time-evolved operator $\Pi_\gamma^m(t)$, up to normalization. Since $\text{Tr}[\Pi_\gamma^m] \neq 1$, we rescale the operator as

$$\Pi_\gamma^m = \text{Tr}[\Pi_\gamma^m] \tilde{\Pi}_\gamma^m, \quad (\text{D3})$$

where $\tilde{\Pi}_\gamma^m$ has unit trace. This ensures that $\langle \rho_\delta^n \rangle_{\gamma,t}^m$ behaves like an expectation value over a normalized observable.

The maximal rate of change of expectation values under unitary dynamics is determined by the SLD operator L_γ^m associated with the observable Π_γ^m . From the Heisenberg equation of motion,

$$\frac{d}{dt} \Pi_\gamma^m(t) = i[H, \Pi_\gamma^m(t)], \quad (\text{D4})$$

the SLD is introduced via

$$\frac{d}{dt} \Pi_\gamma^m(t) = \frac{1}{2} \{ \Pi_\gamma^m(t), L_\gamma^m(t) \}, \quad (\text{D5})$$

where $\{\cdot, \cdot\}$ denotes the anticommutator. The variance of the SLD, $\Delta L_{m,\gamma}^2$, quantifies the maximal instantaneous rate at which the expectation value of the observable can change, and it is invariant under time evolution [38]:

$$\Delta L_{m,\gamma}^2(t) = \Delta L_{m,\gamma}^2(0), \quad \forall t. \quad (\text{D6})$$

To compute $L_\gamma^m(0)$, we define

$$C = i[H, \Pi_\gamma^m(0)] = \frac{1}{2} \{ \Pi_\gamma^m(0), L_\gamma^m(0) \}, \quad (\text{D7})$$

giving the matrix equation

$$2C = \Pi_\gamma^m L_\gamma^m + L_\gamma^m \Pi_\gamma^m. \quad (\text{D8})$$

Diagonalizing Π_γ^m as

$$\Pi_\gamma^m = \mathcal{V} D \mathcal{V}^\dagger, \quad D = \text{diag}(d_1, d_2, \dots, d_d), \quad (\text{D9})$$

and transforming to this eigenbasis,

$$C' = \mathcal{V}^\dagger C \mathcal{V}, \quad L' = \mathcal{V}^\dagger L_\gamma^m \mathcal{V}, \quad (\text{D10})$$

the SLD equation simplifies to an element-wise relation

$$2C'_{kl} = (d_k + d_l)L'_{kl}, \quad (\text{D11})$$

so that

$$L'_{kl} = \begin{cases} \frac{2C'_{kl}}{d_k + d_l}, & d_k + d_l \neq 0, \\ 0, & d_k + d_l = 0. \end{cases} \quad (\text{D12})$$

The SLD in the original basis is then recovered via

$$L_\gamma^m = \mathcal{V} L' \mathcal{V}^\dagger. \quad (\text{D13})$$

The variance $\Delta L_{m,\gamma}^2$ is computed with respect to the initial state and serves as the key parameter in the speed-limit bound.

We define the *interpolation angle* in terms of the eigenvalues of Π_γ^m . Let x_{\min} and x_{\max} denote the minimal and maximal eigenvalues of Π_γ^m . For any value x of the expectation value, we define

$$\tau(\rho_\delta^n, x) \equiv \arccos \left[\frac{2x - x_{\min} - x_{\max}}{x_{\max} - x_{\min}} \right]. \quad (\text{D14})$$

This represents the *interpolation angle*, quantifying where x lies between the extremal expectation values.

The *distance function* is defined as

$$\tau(\rho_\delta^n, \langle \rho_\delta^n \rangle_{\gamma,t}^m) = \left| \langle \rho_\delta^n \rangle_{\gamma,t}^m - \langle \rho_\delta^n \rangle_{\gamma,0}^m \right|, \quad (\text{D15})$$

which quantifies the separation between the initial and time-evolved expectation values of the projector Π_γ^m . The expectation values can be computed as

$$\langle \rho_\delta^n \rangle_{\gamma,t}^m = \text{Tr}[\rho(t) \Pi_\gamma^m], \quad \rho(t) = U(t)\rho(0)U^\dagger(t). \quad (\text{D16})$$

With this definition, the quantum speed-limit bound reads

$$\tau(\rho_\delta^n, \langle \rho_\delta^n \rangle_{\gamma,t}^m) \geq \tau(\rho_\delta^n, \langle \rho_\delta^n \rangle_{\gamma,0}^m) + \Delta L_{m,\gamma} t, \quad (\text{D17})$$

showing that the growth of the distance is lower bounded by a term linear in time, set by the SLD variance.

To determine the minimal time at which the real part of the KDQ loses positivity, we impose

$$\text{Re}\{q_{\delta,\gamma}^{mn}(T_{\delta,\gamma}^{mn})\} = 0, \quad (\text{D18})$$

corresponding to a target value $x_{\text{target}} = 0$ in the distance function. Substituting into the speed-limit bound gives

$$\tau(\rho_\delta^n, 0) = \tau_{\delta,\gamma,0}^{mn} + \Delta L_{m,\gamma} T_{\delta,\gamma}^{\text{re}}, \quad (\text{D19})$$

where

$$\tau_{\delta,\gamma,0}^{mn} = \tau(\rho_\delta^n, \langle \rho_\delta^n \rangle_{\gamma,0}^m) \quad (\text{D20})$$

is determined from the initial KDQ expectation value. Solving for the minimal time yields

$$T_{\text{QSL}} \equiv T_{\delta,\gamma}^{mn} = \frac{\tau(\rho_\delta^n, 0) - \tau_{\delta,\gamma,0}^{mn}}{\Delta L_{m,\gamma}}. \quad (\text{D21})$$

This provides a rigorous lower bound on the time required for the real part of the KDQ to reach zero, signaling the onset of non-classicality.

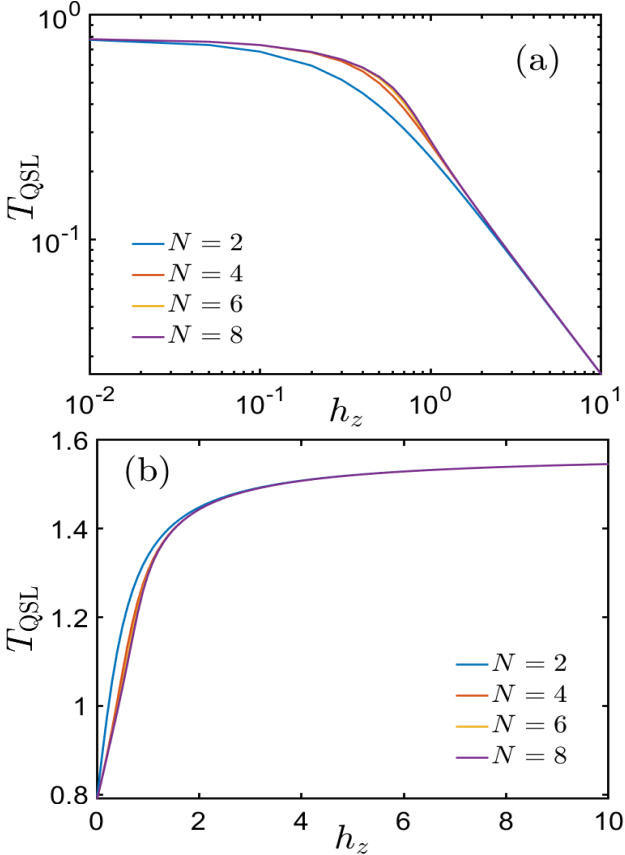


Figure 6. Quantum speed-limit time for different local projector combinations in the integrable transverse-field Ising model. Shown is the time to possible nonpositivity of the real part of the KD quasiprobability, T_{QSL} , as a function of the transverse field h_z for $J = 1$. (a) Projectors of both observables taken as $|1\rangle\langle 1|$. (b) Projectors of both observables taken as $|0\rangle\langle 0|$. In both panels, curves for different system sizes are indicated in the legend.

We evaluate the minimal time for the onset of non-positivity in the real part of the KD quasiprobability using the QSL, denoted as T_{QSL} , for the projector of the observables $W \equiv V = \sigma_1^z$ in the integrable TFIM. Specifically, we consider two distinct combinations of projectors for W and V , where both projectors are either $|1\rangle\langle 1|$ or $|0\rangle\langle 0|$. The QSL time T_{QSL} is computed as a function of the transverse field strength h_z for various system sizes N . When both observables are projected onto $|1\rangle\langle 1|$, T_{QSL} exhibits a trend closely following the behavior of the FTN across all system sizes, as illustrated in Fig. 6(a), albeit with systematically smaller values, reflecting the QSL as a lower bound on the onset of negativity. In contrast, for projectors $|0\rangle\langle 0|$, the time to non-positivity displays a markedly different dependence: T_{QSL} is initially small at weak transverse fields, increases with h_z , and eventually saturates at a finite value [Fig. 6(b)]. Notably, despite the existence of a finite QSL bound in this case, the KD quasiprobability remains strictly non-negative. This observation underscores an important conceptual point: a finite T_{QSL} indicates only the fundamental minimal timescale permitted by the system dynamics, but it does not guarantee the actual emergence of negativity, which depends sensitively on the choice of projector and the underlying Hamiltonian structure.